

# The NICMOS snapshot survey of nearby galaxies

T. Böker<sup>1</sup>, D. Calzetti, W. Sparks, D. Axon<sup>1</sup>, L. E. Bergeron, H. Bushouse, L. Colina<sup>1</sup>, D. Daou, D. Gilmore, S. Holfeltz, J. MacKenty, L. Mazzuca, B. Monroe, J. Najita, K. Noll, A. Nota<sup>1</sup>, C. Ritchie, A. Schultz, M. Sosey, A. Storrs, A. Suchkov (the STScI NICMOS group)  
*Space Telescope Science Institute, 3700 San Martin Drive, Baltimore, MD 21218, U.S.A.*

## ABSTRACT

We present “snapshot” observations with the NearInfrared Camera and MultiObject Spectrometer (NICMOS) on board the Hubble Space Telescope (HST) of 94 nearby galaxies from the Revised Shapley Ames Catalog. Images with 0.2'' resolution were obtained in two filters, a broad-band continuum filter (F160W, roughly equivalent to the H-band) and a narrow band filter centered on the Pa  $\alpha$  line (F187N or F190N, depending on the galaxy redshift) with the 51'' $\times$ 51'' field of view of the NICMOS camera 3. A first-order continuum subtraction is performed, and the resulting line maps and integrated Pa  $\alpha$  line fluxes are presented. A statistical analysis indicates that the average Pa  $\alpha$  surface brightness **in the central regions** is highest in early-type (Sa-Sb) spirals.

*Subject headings:* infrared:galaxies—infrared:ISM:lines and bands—galaxies:nuclei—galaxies:starburst—galaxies:statistics

---

<sup>1</sup>Affiliated with the Astrophysics Division, Space Science Department, European Space Agency

## 1. Introduction

NICMOS is a second generation HST instrument, installed during the HST servicing mission in February 1997. It extends the wavelength region accessible for imaging and spectroscopy with HST to the near infrared (NIR), up to  $\lambda = 2.5 \mu\text{m}$ .

Shortly after its on-orbit installation, it was discovered that the NICMOS dewar suffered from a thermal anomaly that led to a higher than expected sublimation rate of the solid nitrogen coolant, and thus a shorter than anticipated lifetime. In addition, the mechanical deformation of the dewar prevents parafocality of the three NICMOS cameras, to the extent that NIC3, the camera with the widest field of view ( $51'' \times 51''$ ), can only be brought fully to focus by moving the secondary mirror of the HST. This, on the other hand, prevents observations with the other HST instruments which is why it was decided to concentrate all approved NIC3 observations in “campaigns” of 2-3 weeks duration. Two of these campaigns have been successfully executed half a year apart to allow all-sky access.

In order to fill any gaps in the observing schedule during the NIC3 campaigns with meaningful scientific data, a “snapshot” survey was proposed and approved to be undertaken with Director’s discretionary time (proposal ID 7919). The data were made public soon after the observations, and can be retrieved from the HST archive. The scientific rationale behind the project was to obtain wide field imaging of the Pa  $\alpha$  emission for as many galaxies of the Revised Shapley Ames Catalog (RSA, Sandage & Tammann 1987) as allowed by the scheduling efficiency of the NIC3 campaigns.

Since the NIR is much less affected by dust extinction than optical wavelengths, the NIR is well suited for probing the heavily obscured central regions of spiral galaxies. The Pa  $\alpha$  line at  $1.875 \mu\text{m}$  is a recombination line of atomic hydrogen, and as such is indicative of the ionized matter around hot, newly formed stars or active galactic nuclei (AGN). It lies in a wavelength region subject to strong atmospheric absorption by H<sub>2</sub>O molecules and is therefore accessible for ground-based observations only with great difficulty. NICMOS provides two narrow band filters in the NIC3 camera that are suitable for Pa  $\alpha$  observations: the F187N filter was used for all galaxies with a radial velocity  $v_r$  between -1295 and 943  $\text{km/s}$ , while galaxies with  $3181 \leq v_r \leq 4780 \text{ km/s}$  were observed

with the NIC3 F190N filter. The velocity range was chosen such that the Pa  $\alpha$  line falls well inside the high transmission region of the respective filter, with only minor corrections ( $\leq 5\%$ ) needed to account for the highest velocities with respect to the filter central wavelength.

For continuum subtraction, each galaxy was also observed in the F160W filter which approximately spans the H-band from 1.4 - 1.8  $\mu\text{m}$ .

## 2. The sample

The galaxy sample was selected at random from the RSA according to scheduling convenience. Ninety-four galaxies were observed in total, 64 of which lie in the low redshift range, and 30 in the higher. Sorted by Hubble type, the sample contains 17 galaxies classified as E or S0, 20 Sa/Sab/Sb’s, 39 Sbc/Sc’s, and 18 Scd/Sd/Sm/Irregulars. The sample thus should be large enough to be a fair representation of the RSA and its distribution of Hubble type and luminosity. Table 1 lists the observed galaxies.

## 3. Observations and data reduction

The observations were performed using the MULTIACCUM STEP64 sampling sequence as described in the NICMOS instrument handbook (MacKenty *et al.* 1997). All F160W continuum images were taken with NSAMP=11 for a total integration time of 192 s. The F187N and F190N line emission images had values for NSAMP between 13 and 25, yielding integration times between 320 s and 1088 s. Column 5 of Table 1 contains the narrow band integration time.

For data reduction, the calibrated (\*\_cal.fits) FITS images as retrieved from the HST archive were used as a starting point. These images have been dark-subtracted, flatfielded, and cosmic ray corrected in an automated way during the CALNICA pipeline processing as described in the HST data handbook (Voit 1997). The resulting images show a number of residual anomalies, which are described in the following sections.

### 3.1. Bad pixels

Residual bad pixels in the CALNICA processed image are due to three possible defects:

1. Remaining cosmic ray hits that are not detected by the CALNICA pipeline.
2. Defective (i.e. “hot” or “dead”) pixels on the NIC3 detector are also not replaced during pipeline processing because the images were not dithered and no meaningful observational data exist for these pixels.
3. Caused by mechanical contact due to the NICMOS dewar anomaly, small flecks of anti-reflective paint have been scraped off one of the optical baffles. Some of these have migrated onto the NICMOS detector surfaces. These flecks, known as “grot”, result in small areas (one to a few pixels) of reduced sensitivity. Since the grot might be subject to unpredictable movement on the detector, it is currently not included in the bad pixel mask for CALNICA. However, recent results have shown that the grot has been quite stable over time, and plans exist to include the affected pixels in the next version of the CALNICA bad pixel masks.

Since the point-spread-function (PSF) is undersampled in the NIC3 camera, it is not straightforward to discriminate between uncorrected bad pixels and real point sources in the pipeline processed data. We created a mask that defined as bad all pixels that showed a deviation greater than  $4\sigma$  in at least 10% of the images. Since real point sources (and - unfortunately - remaining cosmic ray hits) should appear randomly in the field, this ensures that only systematically bad pixels are included in the mask. All masked pixels were then replaced with the median value of their neighboring pixels. No attempt has been made to correct for the remaining cosmic rays.

### 3.2. Pedestal effect

The so-called “pedestal effect” is a residual DC offset that appears in an image after the dark current subtraction during CALNICA processing. The dark current reference files that are used by CALNICA are not a perfect representation of the actual instrumental bias and dark current, because some or all of the components that contribute to the dark signal are time variable. These variations are believed to be driven by subtle temperature changes in the electronics and/or the detectors themselves. Typical pedestal amplitudes are a few data numbers (DN) up to about

15 DN, but larger values have been occasionally observed.

The effect of a residual bias in the image after dark current subtraction is that multiplication with the flatfield reference file leaves an imprint of the relative pixel sensitivities in the resultant image. To further complicate the matter, the four quadrants of each NICMOS detector have separate amplifiers and read-out electronics. Therefore the pedestal typically is different in each quadrant of a NICMOS image.

To correct the data for the pedestal effect, we have used code developed at STScI by R. van der Marel. The code assumes a constant bias in each detector quadrant, which is a good approximation in most cases. In brief, the program determines the value of this bias by minimizing the spread of the pixel values in each quadrant. The rationale behind this method is that any non-zero bias increases the spread because the image is multiplied by the (inverse) flatfield during CALNICA processing. The software and a description of the algorithms used are available from the WWW<sup>2</sup>. For fields that are largely filled by the science object, as is the case for the dataset presented here, the method of spread minimization performs better than other methods like simple median subtraction or large-scale structure removal.

After the bias value has been determined for each quadrant, the scaled flatfield is subtracted from the image, and the four quadrants are brought to match. The last step is difficult to do in an automated way, especially if the galaxy nucleus — which typically has a very steep gradient in its signal — is located close to quadrant borders. Any residual “edges” in the images presented in §4 are due to shortcomings in the quadrant equilization step and can be improved manually by adding small constants to each quadrant.

### 3.3. Continuum subtraction

To subtract the continuum underlying the Pa  $\alpha$  line emission in the narrow band filter images, the following approach was taken:

Both the F160W and F187N/F190N images were rebinned to a size of  $128 \times 128$  pixels for the purpose of reducing both the scatter and the total number of datapoints in the plot. We then plotted the intensity (in DN) of each pixel in the rebinned F160W image versus that of the same pixel in the rebinned

<sup>2</sup><http://sol.stsci.edu/~marel/software/pedestal.html>

F187N/F190N image. If the galaxy had constant color over the field of view and no Pa $\alpha$  emission, the relation should be linear down to the noise level. Deviations from the linear relation can be due to intrinsic color variations, differential extinction effects, Pa $\alpha$  line emission, or a combination thereof.

We then performed a linear least squares fit to the data points, the slope of which should be the scaling factor between the two filters. In most cases, all pixels were used for the fit, excluding the bottom 10 rows in the original images, since these are subject to vignetting and contain no reliable information. In addition, the 500 brightest pixels in the F187N/F190N image were excluded, because those pixels typically contain either foreground stars, bright HII regions, or the galaxy nucleus. Therefore they do not provide a good estimate for the average color of the image. Finally, the F160W image was scaled by the slope of the linear fit, and the result subtracted from the F187N/F190N image in order to obtain a map of the excess emission. Although it is not possible to discriminate between the various contributions to the excess emission, as mentioned above, we refer to the resulting images as Pa $\alpha$  maps for the remainder of this paper in order to simplify the terminology. We also point out that if a smoothly distributed component of Pa $\alpha$  emission is present, it will be removed by this procedure, thus leading to an underestimate of the total Pa $\alpha$  flux. Also, no attempt was made to correct for the PSF differences between the two filters because the NIC3 PSF is undersampled in both filters.

Fig. 1 contains the F160W images, the Pa $\alpha$  maps, and the fit results for all galaxies of the sample after the described data reduction. The plot of the flux distribution gives a visual impression of the complexity of the galaxy color distribution or, correspondingly, the reliability of the continuum scaling factor. For most early type galaxies, e.g. NGC 2314 or NGC 2681, the scatter around the linear best fit is small. In principle, a higher fraction of ionized gas causes larger scatter. In nearby galaxies where many individual stars are resolved (e.g. NGC 247 or NGC 4144), the scatter is largest because of the color distribution of the stars. However, a mere shift of the solid line indicating the best fit does not affect the quantitative results. This is because a possible offset is removed when measuring the Pa $\alpha$  signal, as described in § 3.4

Based on the Pa $\alpha$  images of Fig. 1, a rough mor-

phological classification of the galaxy sample was performed. In column 8 of Table 1, each galaxy is labeled according to the presence of one or more of the following features: unresolved or extended Pa $\alpha$  emission from the galaxy nucleus (N), individual HII regions located in a spiral arm structure (S), a ring (R), or isolated throughout the disk (I), diffuse nebulosities (DN), or prominent dust lanes (DL). For most of these labels, we feel confident that they indeed contain information on the distribution of real Pa $\alpha$  emission. The only exception is the often observed signal from the nucleus of the galaxy. Whether this is true Pa $\alpha$  emission or the effect of a color gradient can only be answered with additional spectral information. A slight spatial offset between the two images or the small PSF differences between the filters might also lead to residual asymmetric signal in the nuclei, if they have very steep brightness profiles. However, the edge-like color gradients observed in some nuclei like NGC 2683 or NGC 4373 are probably real, since stars in the field subtract out almost perfectly, and the structure is too extended to be caused by PSF mismatches. In summary, the label N in Table 1 indicates that the Pa $\alpha$  image shows increased signal in the nucleus without specifying its nature.

A number of objects show an obvious oversubtraction in the nucleus. This is a direct consequence of the simplistic “one-color” approach taken here if the continuum emission in the center has a bluer color than in the disk. The most likely explanations for a bluer color of the nucleus are enhanced star star formation or the presence of an AGN. A more detailed case-by-case study, possibly with additional color information, should allow a better continuum subtraction in the nuclei, but is beyond the scope of this paper due to the large data volume.

### 3.4. Pa $\alpha$ fluxes

In order to compare the star formation properties of the galaxy sample, the integrated Pa $\alpha$  flux was calculated from the line maps. A first step checked for any systematic offsets in the maps by calculating the mode of pixel values in an empty region of the Pa $\alpha$  map. The mode should be close to zero after the described data reduction procedure, if the linear fit for the continuum was correct. In cases where a (small) offset was present, the mode was subtracted to bring the Pa $\alpha$  “background” to zero.

An automated method was developed to sum the total Pa $\alpha$  flux in the line maps which is briefly de-

scribed here. Continuum oversubtraction would seriously affect the result when simply adding all pixels in the Pa  $\alpha$  map. The image was therefore clipped at a certain threshold and only the signal above this level was summed. One complication to this method is that some images have a number of pixels above the noise level that apparently do not contain true line emission. This is particularly true for images that were taken after an HST passage through the South Atlantic Anomaly (SAA). The effect of a cosmic particle hit on the NICMOS detectors is equivalent to a higher dark current in the affected pixels. Therefore, when defining the threshold, we had to compromise between clipping at a high level, thus potentially losing real Pa  $\alpha$  signal, or including more noise in the number for Pa  $\alpha$  flux. For images that contained extended Pa  $\alpha$  emission, we found that a  $2\sigma$  threshold would not lose a significant amount of Pa  $\alpha$  signal, while eliminating most - but not all - of the noisy pixels. Therefore, all images were clipped at the  $2\sigma$  level, i.e. pixels below this threshold were set to zero, and the total remaining flux in the image calculated. A possible remaining noise contribution and the uncertainty regarding the signal nature described in §3.3 could lead to an overestimate of the true Pa  $\alpha$  flux. On the other hand, any Pa  $\alpha$  contribution below the  $2\sigma$  level will be missed by our method, as well as a smooth, extended component.

Such a diffuse Pa-alpha emission is known to be present in at least some early type galaxies, and virtually all ellipticals and S0's for which optical spectra are available are classified as LINERs (Goudfrooij 1998). However, the exact physical mechanism behind the gas ionization is still unclear. Several possibilities, including shocks, post-AGB stars, cooling flows, and a low luminosity AGN could be at work, but, contrary to spirals and irregulars, a recent star formation is discarded (Goudfrooij 1998). Thus, the removal of a possible diffuse component will not affect any conclusions on star formation activity.

We estimate the uncertainty in the numbers of Table 1 to be between 10 and 30%, depending on the noise level. We made no attempt to correct for the position of the line with respect to the central wavelength of the narrow-band filter, because the required corrections would not contribute significantly to the described uncertainties, as explained in § 1.

## 4. Results

This survey is an unbiased sample of galaxies closer than  $v_z \sim 5000$  km/s, and should therefore be representative of the local universe. In particular, the combination of narrow and broad band filters reveals the Pa  $\alpha$  emission and should give us an unobscured view of star formation in the neighborhood of the Milky Way. Because of the large data volume, no attempt was made to address spatial color gradients (see § 3.3). However, a more detailed analysis on a case-by-case basis should be possible, e.g. by comparing Pa  $\alpha$  equivalent widths with predictions from stellar population synthesis models. A few general comments can still be made from the images alone.

### 4.1. Star formation in the galaxy disks

From the images in Fig. 1, it is evident that Pa  $\alpha$  emission in the disks of most spiral galaxies traces the spiral arm structure. This is expected since the denser environment in the spiral arms is known to cause enhanced star formation. The line emission is clumpy, unlike the generally smooth stellar continuum. This matches similar results obtained at ultraviolet wavelengths which also trace active star formation (e.g. Waller *et al.* 1997). However, the UV morphology is hampered by strong dust extinction. The question is whether star formation is clumpy because of how stars form or because of how dust obscures. In this context, the relatively dust-insensitive Pa  $\alpha$  morphology in our images confirms earlier claims that star formation is intrinsically clumpy. Early type galaxies generally show little or no line emission in their disks, but often have strong emission from their central regions. A notable exception is NGC 1241, an Sb spiral with a Sy 2 nucleus, which shows an inclined ring of star formation about  $7''$  in diameter surrounding the nucleus. At the distance of the galaxy (80 Mpc for  $H_o=50$  km/s/Mpc), this corresponds to 2.7 kpc.

The clumps of Pa  $\alpha$  emission lose their organized distribution when going from late type spirals to irregular galaxies, and their typical size becomes larger. The strongest Pa  $\alpha$  emission is found in starburst galaxies like NGC 3077, NGC 3593, or NGC 4449, to name a few. A special case is NGC 1705. This metal-poor, almost dust-free dwarf galaxy contains a very UV bright super star cluster, which has very little nebular gas emission (Meurer *et al.* 1995). This is an effect of the cluster age of about 13 Myr. At this stage, the hottest cluster stars are no longer ion-

izing the surrounding interstellar matter. However, the strong stellar winds observed to come out of the galaxy are believed to be a consequence of the past activity of the cluster (Heckman & Leitherer 1997). They might also be responsible for the extended, low-level star formation in the outer regions of the galaxy that is evident in the Pa  $\alpha$  image.

A number of highly inclined galaxies in the sample show strong dust lanes even in the NIR. Examples are NGC 891, and also NGC 2683 and NGC 5908. The dust lane in NGC 891 is so opaque that the differential extinction in the two filters causes strong residual signal in the Pa  $\alpha$  map. This extreme case demonstrates the problem of disentangling color effects from true line emission.

#### 4.2. Pa $\alpha$ surface brightness and star formation rates

It is customary to use the surface brightness (SB) of hydrogen recombination lines, in particular the H  $\alpha$  line, as a measure for the star formation rate of the galaxy. Studies along these lines at UV and optical wavelengths (e.g. Kennicutt 1983, Kennicutt & Kent 1983, Deharveng *et al.* 1994, Young *et al.* 1996) resulted in the notion that star formation in later Hubble types is on the average higher than in earlier types.

These studies were performed over apertures that included the whole visible disk of the galaxy. In contrast, the NIC3 field of view of  $51'' \times 51''$  in all cases does not contain the full disk, especially for the nearby galaxies. This is evident from column 7 of Table 1 which lists the ratio  $D_{25}$  to the NIC3 field of view. Since it is unknown what fraction of the total Pa  $\alpha$  emission lies outside the NIC3 field, it is not possible to derive the average SB<sub>Pa $\alpha$</sub>  over the whole galaxy disk. Therefore, one can only draw conclusions for the central  $51''$  of the galaxies, and thus might expect slightly different results for the variation of star formation rate with Hubble type than derived from the earlier studies. The Pa  $\alpha$  flux from Table 1 was converted into an average surface brightness **over the NIC3 field** according to

$$SB_{Pa\alpha} [L_{\odot}/pc^2] = 5 \cdot 10^{18} \cdot F_{Pa\alpha} [W/cm^2]. \quad (1)$$

Here, the constant  $5 \cdot 10^{18}$  results purely from unit conversions, the mean value of SB<sub>Pa $\alpha$</sub>  is independent of galaxy distance. Following the approach of Young *et al.* (1996), each of the four panels in Fig. 2a contains histograms of SB<sub>Pa $\alpha$</sub>  for the full sample of 94

galaxies (dashed line) in comparison to a subset of Hubble types, namely (i) E - S0, (ii) Sa - Sb, (iii) Sbc - Sc, and (iv) Scd - Irr. The median SB<sub>Pa $\alpha$</sub>  for all galaxies in the respective subset is indicated by a star symbol. As found by the earlier studies, the scatter in the histograms is large. We also confirm the generally low star formation activity in Ellipticals and S0s, about an order of magnitude fainter than the values found for spirals and irregulars.

As for the spirals and irregulars in our sample, we do not see the monotonic increase of SB<sub>Pa $\alpha$</sub>  between Sa and Sm that Young *et al.* (1996) found for H  $\alpha$ . Rather, we find that SB<sub>Pa $\alpha$</sub>  **decreases** slightly between Sa and Sm. This result remains basically unchanged if all galaxies with redshifts above  $945 \text{ km/s}$  (those observed with the F190N filter) are excluded (Fig 2b). For the full sample, Sa's to Sb's show a median (mean) SB<sub>Pa $\alpha$</sub>  that is 53% (64%) higher than Sbc's and Sc's.

The images of our sample are dominated by the central regions of the galaxies. This follows from the fact that the average  $D_{25}$  is larger than the field-of-view (9.1 times the NIC3 field for the F187N sample, compared to 2.7 for the F190N sample, see column 7 in Table 1). Therefore, our finding of a higher SB<sub>Pa $\alpha$</sub>  in the centers of early-type galaxies can be understood if the fraction of ionized gas in their nuclei is higher than in late types. A similar notion was made by Young *et al.* (1996) who also found that a substantial fraction of the H  $\alpha$  emission in early Hubble types stems from the nucleus. This result can be interpreted as a direct consequence of the more likely existence of an AGN in early-type spirals. A large fraction of the early-type (Sbc or earlier) galaxies in our sample (15 out of 47) show indications of a Seyfert- or LINER-type nucleus, while only a small fraction (2 out of 47) of late types (Sc or later) are classified as AGNs. Thus, if a compact AGN exists preferentially in the core of early-type spirals, its contribution would increase the ionized gas fraction relative to a galaxy without an AGN. Therefore, this result does not mean that nuclear star formation is weaker in late-type spirals but reflects the observational result that luminous AGNs avoid late spirals and irregulars, as found by Ho, Filippenko & Sargent (1997b). In fact, many Sc's or Sd's reveal signs of massive gaseous inflow towards their nuclei, as will be shown in the next section.

### 4.3. Nuclear star formation and gas dynamics

Active star formation occurs in regions where the molecular gas is dense enough to become gravitationally unstable. The strong star formation that is often observed in the nuclear regions of galaxies requires some mechanism that causes large amounts of molecular gas to fall into the central few hundred parsecs of the galaxy.

The most commonly evoked process by which the gas can lose its angular momentum is that of dynamical resonances of the gas orbits in the non-axisymmetric potential of a stellar bar. Various compelling theoretical arguments indicate that bars in galaxies are indeed an efficient mechanism for channeling gas from the outer to the nuclear regions of spirals (Shlosman, Begelman, & Frank 1990, Athanassoula 1992, Buta & Combes 1996). According to these models, nuclear star-forming rings and disks are expected by-products of gas inflow towards the inner regions in barred spirals at the locations of the inner Lindblad resonances (ILRs). These nuclear rings are also thought to be an integral part of the gas dissipation processes which ultimately lead to the fueling of AGNs and possibly to the formation of central black holes. Massive nuclear disks are themselves subject to non-axisymmetric dynamical instabilities which drive the gas further inwards by means of gravitational torques, possibly leading to the formation of nested bars and fueling stellar and nonstellar activities in the center (Shlosman, Frank, & Begelman 1989).

The unprecedented spatial resolution of the NICMOS data allows to investigate such processes in more distant galaxies than possible from ground-based observations. Figure 3 contains a collection of some of the more interesting galaxies in our sample that reveal complex gas distributions like double peaks, spirals, bars, rings or arcs in the Pa $\alpha$  images. All of them are Sbc or later spirals. In Fig. 3, we compare the Pa $\alpha$  (in grayscale) and continuum (contours) emission from the nuclear region. To emphasize the extended structure, all images have been median filtered over a 3 $\times$ 3 box. In many cases in Fig. 3, like, e.g., NGC 2989, NGC 6754, or NGC 6946, the continuum contours are elongated. This is unlikely a pure projection effect, and emphasizes that the prominent stellar bars found in many early-type spirals can indeed have weaker counterparts in late Hubble types. High spatial resolution NIR studies, together with molec-

ular line observations of a number of nearby galaxies like e.g. M 83 (Handa *et al.* 1990, Gallais *et al.* 1991), NGC 253 (Peng *et al.* (1996), Böker, Krabbe, & Storey 1998), NGC 4570 (van den Bosch & Emsellem 1998), or IC 342 (Ishizuki *et al.* 1990, Böker, Förster-Schreiber, & Genzel 1997), have shown that massive gas inflows — presumably triggered by dynamical resonances with a stellar bar — fuel active star formation in the central few tens of parsecs. It is likely that the gas morphologies seen in Fig. 3 are caused by similar processes.

### 5. Summary

We have presented near infrared continuum and Pa $\alpha$  images of the centers of 94 nearby galaxies of all morphological types. The unprecedented spatial resolution of the data reveals remarkable activity and a wealth of structure in many of the galaxies.

We have mapped the gas morphology in the galaxy nuclei and found in many cases evidence for gas infall, most likely triggered by dynamical interaction with a stellar bar. We also have performed a statistical analysis of the average Pa $\alpha$  surface brightness  $SB_{Pa\alpha}$  over the NIC3 field. The main result is that  $SB_{Pa\alpha}$  **in the central regions** is on the average stronger in Sa and Sb galaxies than in later Hubble types, most likely due of the higher fraction of AGN in early type spirals.

The catalog is intended to serve as a database for further study of individual objects, their star formation activity, dynamics, and matter distribution. The data are available electronically from the HST archive (Prop. 7919), and we encourage all interested colleagues to take advantage of them.

We are grateful to our anonymous referee whose comments helped a great deal to improve the quality of this paper. This research has made use of the NASA/IPAC Extragalactic Database (NED) which is operated by the Jet Propulsion Laboratory, California Institute of Technology, under contract with the National Aeronautics and Space Administration.

## REFERENCES

- Athanassoula, E. 1992, MNRAS 259, 345
- Böker, Krabbe, A., & Storey, J.W.V. 1998, ApJ, 498, L115
- Böker, T., Förster-Schreiber, N., & Genzel, R. 1997, AJ, 114, 1883
- Buta, R., & Combes, F. 1996, Fund. of Cosmic Phys. 17, 95
- Deharveng, J. M., Sasseen, T. P., Buat, V., Bowyer, S., Lampton, M., & Wu, X. 1994, A&A , 289, 715
- de Vaucouleurs, G., de Vaucouleurs, A., & Corwin, H.G. 1976, Second Reference Catalogue of Bright Galaxies (University of Texas Press, Austin)
- Gallais, P., Rouan, D., Lacombe, F., Tiphéne, D., & Vauglin, I. 1991, A&A , 243, 309
- Goudfrooij, P. 1998, to appear in “Star Formation in Early-type Galaxies”, PASP Conf. Series
- Handa, T., Nakai, N., Sofue, Y., & Hayashi, M. 1990, PASJ, 42, 1
- Heckman, T. M. & Leitherer, C. 1997, AJ, 114, 69
- Ho, L. C., Filippenko, A. V., & Sargent, W. L. W. 1997a, ApJS, 112, 315
- Ho, L. C., Filippenko, A. V., & Sargent, W. L. W. 1997b, ApJ, 487, 568
- Ishizuki, S., Kawabe, R., Ishiguro, M., Okumura, S. K., Morita, K.-I., Chikada, Y., & Kasuga, T. 1990, Nature, 344, 224
- Kennicutt, R. C. 1983, ApJ, 272, 54
- Kennicutt, R. C. & Kent, S. M. 1983, AJ, 88, 1094
- MacKenty, J.W., *et al.* 1997, “NICMOS Instrument Handbook”, Version 2.0 (Baltimore: STScI)
- Meurer, G. R., Heckman, T. M., Leitherer, C., Kinney, A., Robert, C., & Garnett, D. R. 1995, AJ, 100, 2665
- Peng, R., Zhou, S., Whiteoak, J. B., Lo, K. Y., & Sutton, E. C. 1996, ApJ, 470, 821
- Sandage, A. & Tammann G. A. 1987, “A revised Shapley-Ames Catalog of bright Galaxies”, 2nd ed., Carnegie Institution of Washington Publication (Washington, D.C.)
- Shlosman, I., Frank, J., & Begelman, M.C. 1989, Nature, 338, 45
- Shlosman, I., Begelman, M.C., & Frank, J. 1990, Nature, 345, 679
- van den Bosch, F. C. & Emsellem, E. 1998, MNRAS, 298, 276
- Voit, M. (Editor) 1997, “HST Data Handbook, Vol. I”, Version 3.0 (Baltimore: STScI)
- Veron-Cetty, M. P. & Veron, P., 1998, “Quasars and Active Galactic Nuclei” (8th Ed.), ESO Sci. Rep. 18, 1
- Waller, W. *et al.* 1997, ApJ, 481, 169
- Young, J. S., Allen, L., Kenney, J. D. P., Lesser, A., & Rownd, B. 1996, AJ, 112, 1903

## Figure captions

Fig. 1.— F160W image (top), Pa  $\alpha$  image (center), and results of the continuum fit (bottom) for all galaxies of the sample. North and east are indicated in the upper right corner of the F160W image. The field of view for all images is  $51'' \times 51''$ , the resolution is  $0.2''$ . In the plots, the 100 brightest pixels in the F160W are not shown to optimize the plot range.

Fig. 2.— Histograms of the Pa  $\alpha$  surface brightness for various Hubble types. a) Results for the full sample. b) Results for only those galaxies with redshifts less than  $945 \text{ km/s}$ . For each histogram, the results for the full sample of 94 galaxies is indicated by the dashed line for comparison. The median SB for all galaxies in the respective subset is indicated by a star symbol.

Fig. 3.— Overlay of the Pa  $\alpha$  (grayscale) and continuum (contours) emission of the central regions for nine sample galaxies with central gas concentrations. The images have been median filtered over a  $3 \times 3$  box.

---

This 2-column preprint was prepared with the AAS L<sup>A</sup>T<sub>E</sub>X macros v4.0.



TABLE 1  
THE SAMPLE

NGC	type	AGN?	$v_z$ [km/s]	$t_{\text{int}}$ [s]	$F_{\text{Pa}\alpha}$ [ $10^{-21}\text{W}/\text{cm}^2$ ]	$\frac{D_{25}}{51^{\prime\prime}}$	Pa $\alpha$ ?
128	S0(8)pec		4253	896*	< 0.1	3.5	–
151	SBbc(rs)		3741	704*	10.6	4.4	R/S,N
214	Sbc(r)		4499	704*	12.0	2.2	S,N
221 (M 32)	E2		-200	832	46.7	10.3	–
237	Sc(s)	S? <sup>2</sup>	4139	768*	18.5	1.9	S
247	Sc(s)		156	448	8.2	25.3	I
404	S0(0)	L2 <sup>1</sup>	-39	576	16.8	4.1	N
491	SBbc(r)		3899	704*	43.8	1.7	S
598 (M 33)	Sc(s)	H <sup>1</sup>	-180	896	21.3	83.5	DN
628 (M 74)	Sc(s)		656	576	5.7	12.4	I
672 (VV 338)	SBc(s)	H <sup>1</sup>	413	1088	20.0	8.5	I
891	Sb	H <sup>1</sup>	530	960	147.2	15.9	DL
925	SBc(s)	H <sup>1</sup>	564	576	13.1	12.4	I
976	Sbc(r)		4362	512*	22.6	1.8	S,N
1241 (VV 334)	SBbc(s)	S2 <sup>2</sup>	4028	576*	20.2	3.3	S,R,N
1705	Am.		640	576	5.2	2.2	I, DN
2314	E3		3872	704*	9.9	2.0	N
2366 (DDO 42)	SBm		98	1088	6.9	9.6	I
2403	Sc(s)	H <sup>1</sup>	131	640	20.0	25.8	I, DN
2639	Sa	S1.9 <sup>2</sup>	3187	640*	9.6	2.1	R,N
2642	SBb(rs)		4439	576*	9.8	2.4	S,N
2672	E2		3983	384*	< 0.1	3.5	–
2681	Sa	L1.9 <sup>1</sup>	715	576	24.3	4.2	N
2683	Sb	L2/S2 <sup>1</sup>	404	896	32.9	11.0	S,DL,N
2685	S0(7)pec	S2/T2:: <sup>1</sup>	881	704	2.7	5.3	N
2749	E3		4229	896*	5.9	2.0	N
2787	SB0/a	L1.9 <sup>1</sup>	664	960	< 0.1	3.8	–
2841	Sb	L2 <sup>1</sup>	637	768	11.6	9.6	N
2903	Sc(s)	H <sup>1</sup>	550	704	74.5	14.9	R,I, DN, DL
2942	Sc(s)		4414	704*	12.7	2.6	I
2976	Sd	H <sup>1</sup>	13	512	14.4	7.0	I,N
2989	Sc(s)	H2 <sup>2</sup>	4166	960*	6.5	2.0	S,N
2998	Sc(rs)		4777	512*	7.7	3.4	S,I
3077	Am.	H <sup>1</sup>	7	832	66.5	6.4	DN
3184	Sc(r)	H <sup>1</sup>	589	960	6.4	8.7	N,I
3271 (IC 2585)	Sa		3824	1088*	13.1	3.7	N
3275	SBab(r)		3241	640*	16.7	3.3	N
3379 (M 105)	E0	L2/T2:: <sup>1</sup>	893	704	< 0.1	6.4	–
3571 (NGC 3544)	Sa		3777	896*	< 0.1	3.5	–
3593	Sa pec	H <sup>1</sup>	625	320	57.0	6.1	S,R,N
3627 (M 66)	Sb(s)	T2/S2 <sup>1</sup>	723	640	23.5	11.4	N,I
3675	Sb(r)	T2 <sup>1</sup>	762	832	26.1	7.0	S,I
3738	Sd	H <sup>1</sup>	224	896	11.6	3.0	I, DN
3769	SBc(s)		737	512	17.7	3.7	I
3782	SBcd(s)		738	832	6.6	2.0	I

TABLE 1—*Continued*

NGC	type	AGN?	$v_z$ [km/s]	$t_{\text{int}}$ [s]	$F_{\text{Pa}\alpha}$ [ $10^{-21}\text{W}/\text{cm}^2$ ]	$\frac{D_{25}}{51''}$	Pa $\alpha$ ?
IC 749	SBc(rs)		798	896	7.5	2.7	I
IC 750	S(b)		713	1088	94.0	3.1	S
4026	S0(9)		878	768	3.4	6.1	DN
4062	Sc(s)	H <sup>1</sup>	772	576	14.3	4.8	I
4085	Sc		753	768	44.0	3.3	S,N
4102	Sb(r) pec	H <sup>1</sup>	865	704	98.8	3.5	S,N
4111	S0(9)	H <sup>1</sup>	791	896	18.4	5.4	N
4136	Sc(r)	H <sup>1</sup>	445	832	2.4	4.7	S,N
4144	Scd	H <sup>1</sup>	265	704	6.5	7.1	I
4178 (IC 3042)	SBc(s)	H <sup>1</sup>	355	512	13.8	6.0	I
4183	Scd	H <sup>1</sup>	931	576	4.1	7.4	I
4190 (VV 104)	Sm		231	704	6.5	2.0	I,DN
4192 (M 98)	Sb	T2 <sup>1</sup>	-140	640	12.4	11.6	S
4278	E1	L1.9 <sup>1</sup>	630	704	12.2	4.8	N
4293	Sa	L2 <sup>1</sup>	933	768	11.6	6.6	N,I
4294	SBc(s)		352	704	22.8	3.8	S
4299	Sd(s)		232	640	23.5	2.0	I,DN
4373	E(4,2)		3444	896*	8.0	4.0	N
4389	SBc(s)pec		717	896	20.3	3.1	N,I
4395	Sd	S1.8 <sup>2</sup>	317	320	5.2	15.6	N
4417	S0(7)		843	448	< 0.1	4.0	–
4449	Sm	H <sup>1</sup>	207	1024	107.3	7.3	I,DN
4490 (VV 30)	Scd pec	H <sup>1</sup>	570	768	43.1	7.4	N,I,DN
4559	Sc(s)	H <sup>1</sup>	810	576	28.0	12.6	I
4571 (IC 3588)	Sc(s)		343	704	0.3	4.2	I
4605	Sc(s)	H <sup>1</sup>	141	960	17.6	6.8	I,DN
4701	Sbc(s)		724	1024	14.4	3.3	S
4786	E3		4647	704*	10.6	1.9	N
4826 (M 64)	Sab(s)	T2 <sup>1</sup>	413	320	69.1	11.8	S,DL
5055 (M 63)	Sbc(s)	T2 <sup>1</sup>	503	512	45.3	14.9	S,I,DL
5444	E3		3974	960*	4.9	2.8	N
5474 (VV 344)	Scd(s) pec	H <sup>1</sup>	275	576	5.6	5.7	I,DN
5585	Sd(s)	H <sup>1</sup>	304	576	3.2	6.8	I,DN
5605	Sc(rs)		3363	640*	6.4	1.9	I
5641	SBab		4467	576*	3.6	3.0	N
5653	Sc(s) pec		3557	512*	50.4	2.0	S
5908	Sb		3312	384*	33.9	3.8	S,DL
6207	Sc(s)	H <sup>1</sup>	846	832	33.2	3.5	I
IC 4710	SBd(s)		700	448	2.9	4.2	N
6684	SBa(s)		886	768	14.1	4.7	N
6699	Sbc(s)		3509	704*	9.2	1.8	N,S,I
6744	Sbc(r)		833	832	3.4	23.6	N
6754	Sbc(s)		3325	512*	15.4	2.2	N,S,I
6808	Sc(s)		3466	576*	33.0	1.8	S,I
6822 (IC 4895)	Im		-49	512	14.9	18.3	I

TABLE 1—*Continued*

NGC	type	AGN?	$v_z$ [km/s]	$t_{\text{int}}$ [s]	$F_{\text{Pa}\alpha}$ [ $10^{-21}\text{W}/\text{cm}^2$ ]	$\frac{D_{25}}{51''}$	Pa $\alpha$ ?
6876	E3		3971	384*	< 0.1	3.3	–
6946	Sc(s)	H <sup>1</sup>	48	768	109.5	13.6	N,S,I
IC 5052	Sd		307	832	27.0	7.0	I
7309	Sc(rs)		3938	1024*	10.3	2.2	N,S,I

NOTE.—Column 1: NGC No. and possible alternative names. Columns 2 and 4: morphological type and recession velocity, resp., as taken from the RSA (Sandage & Tammann 1987). Column 3: type of nuclear activity, adopted from Ho, Filippenko & Sargent (1997a) (1) or Veron-Cetty & Veron (1998) (2): H II nucleus (H), Seyfert nucleus (S), LINER (L or S3), and transition object (T). Numbers attached to the class letter designate the type; “:” and “::” denote uncertain and highly uncertain classifications. Galaxies that appear in neither of these catalogs have no entry. Column 5: integration time for the narrow band filter (F190N with \*, F187N otherwise). Column 6: total Pa  $\alpha$ -flux in the field of view. Column 7: ratio of optical diameter  $D_{25}$  (taken from the RC2) to the NIC3 field of view of  $51''$ . Column 8: morphology of the excess emission in the Pa  $\alpha$  image, if present: nuclear (N), HII regions in a spiral arm structure (S), a ring (R), or isolated throughout the disk (I), diffuse nebulosities (DN), or dust lanes (DL).

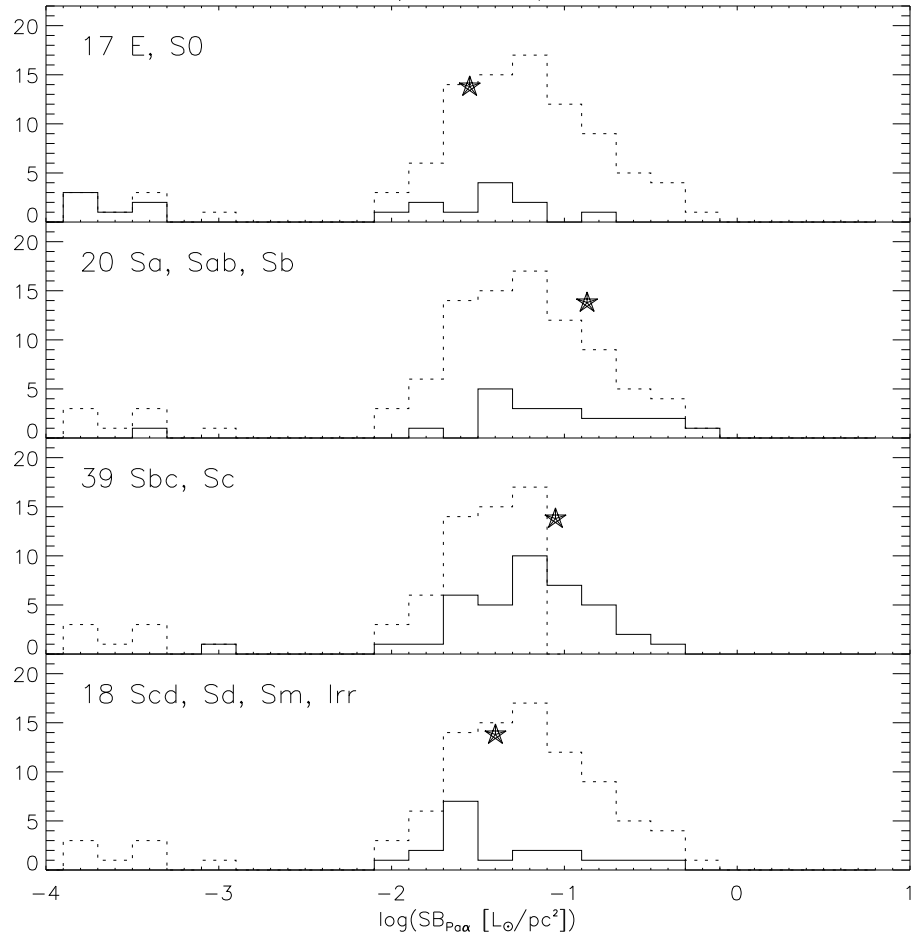
This figure "fig1\_1.jpg" is available in "jpg" format from:

<http://arxiv.org/ps/astro-ph/9903307v2>

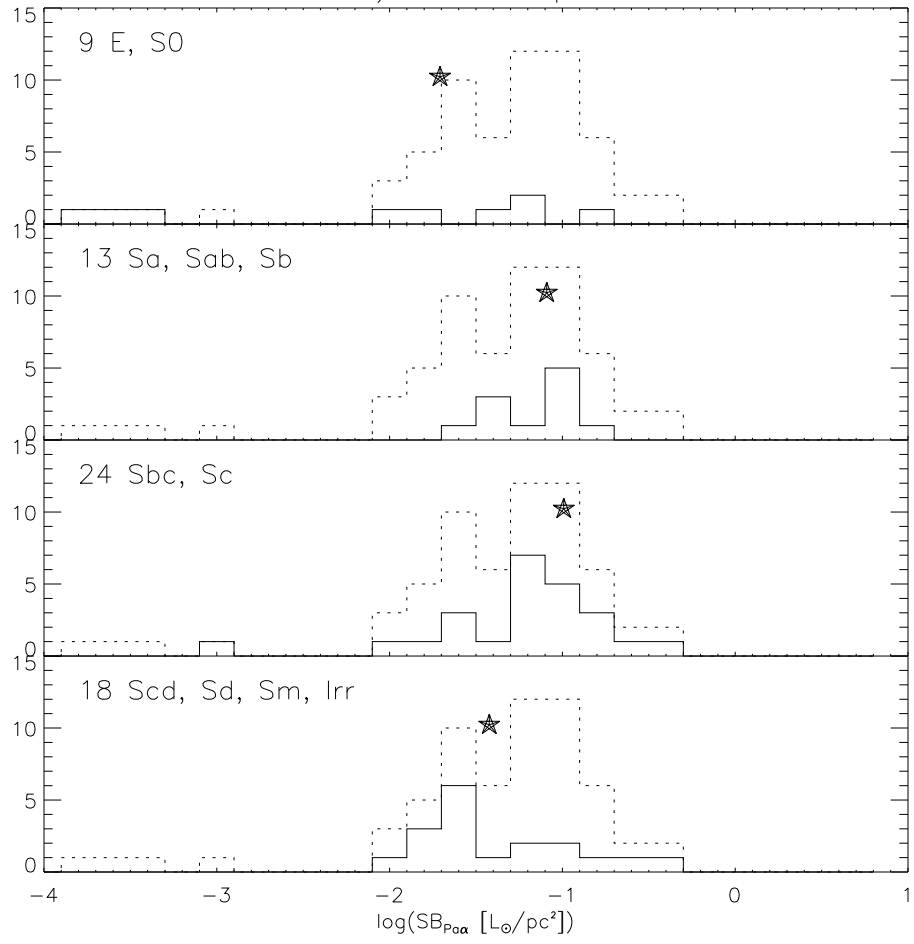
This figure "fig1\_2.jpg" is available in "jpg" format from:

<http://arxiv.org/ps/astro-ph/9903307v2>

a) Full Sample



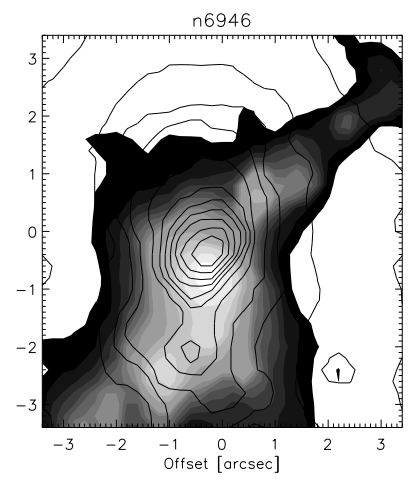
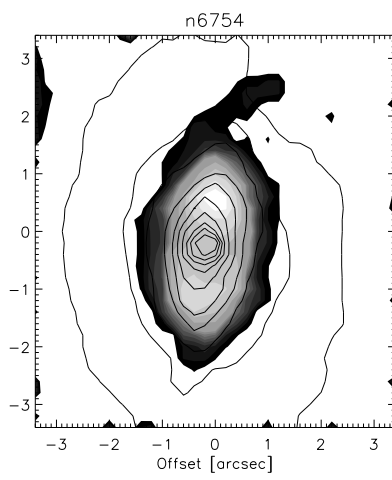
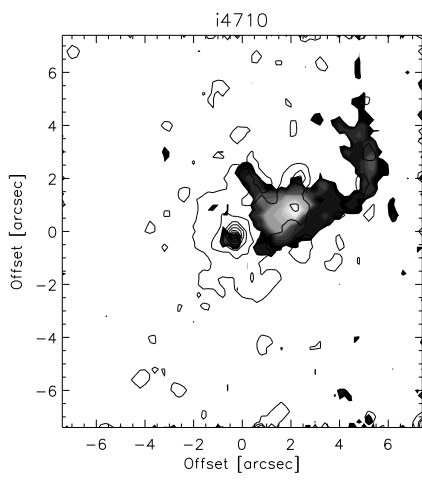
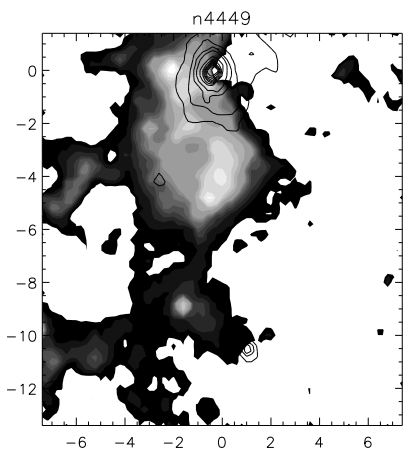
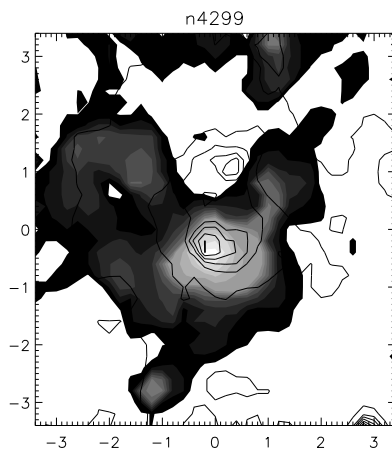
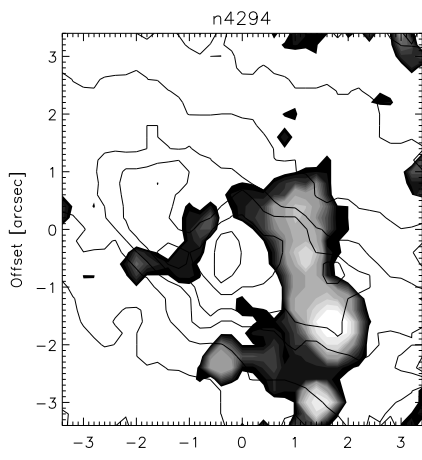
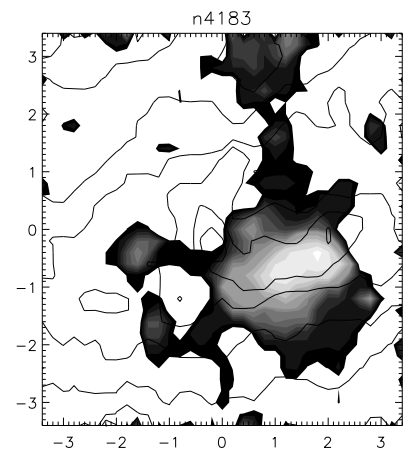
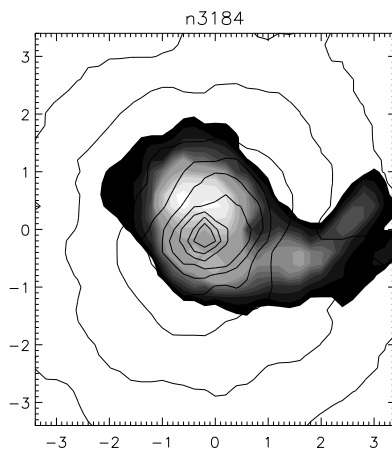
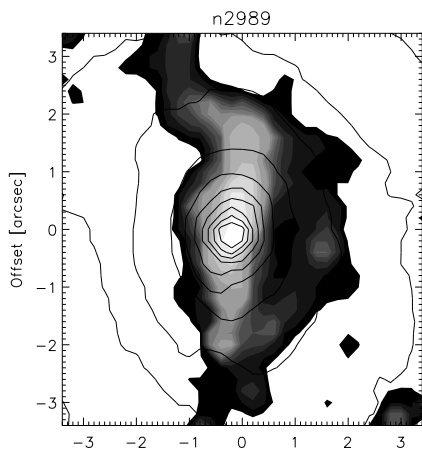
b) F187N Sample



This figure "fig1\_3.jpg" is available in "jpg" format from:

<http://arxiv.org/ps/astro-ph/9903307v2>





This figure "fig1\_4.jpg" is available in "jpg" format from:

<http://arxiv.org/ps/astro-ph/9903307v2>

This figure "fig1\_5.jpg" is available in "jpg" format from:

<http://arxiv.org/ps/astro-ph/9903307v2>

This figure "fig1\_6.jpg" is available in "jpg" format from:

<http://arxiv.org/ps/astro-ph/9903307v2>

This figure "fig1\_7.jpg" is available in "jpg" format from:

<http://arxiv.org/ps/astro-ph/9903307v2>

This figure "fig1\_8.jpg" is available in "jpg" format from:

<http://arxiv.org/ps/astro-ph/9903307v2>

This figure "fig1\_9.jpg" is available in "jpg" format from:

<http://arxiv.org/ps/astro-ph/9903307v2>

This figure "fig1\_10.jpg" is available in "jpg" format from:

<http://arxiv.org/ps/astro-ph/9903307v2>



This figure "fig1\_11.jpg" is available in "jpg" format from:

<http://arxiv.org/ps/astro-ph/9903307v2>

This figure "fig1\_12.jpg" is available in "jpg" format from:

<http://arxiv.org/ps/astro-ph/9903307v2>

This figure "fig1\_13.jpg" is available in "jpg" format from:

<http://arxiv.org/ps/astro-ph/9903307v2>

This figure "fig1\_14.jpg" is available in "jpg" format from:

<http://arxiv.org/ps/astro-ph/9903307v2>

This figure "fig1\_15.jpg" is available in "jpg" format from:

<http://arxiv.org/ps/astro-ph/9903307v2>

This figure "fig1\_16.jpg" is available in "jpg" format from:

<http://arxiv.org/ps/astro-ph/9903307v2>

This figure "fig1\_17.jpg" is available in "jpg" format from:

<http://arxiv.org/ps/astro-ph/9903307v2>

This figure "fig1\_18.jpg" is available in "jpg" format from:

<http://arxiv.org/ps/astro-ph/9903307v2>



This figure "fig1\_19.jpg" is available in "jpg" format from:

<http://arxiv.org/ps/astro-ph/9903307v2>

This figure "fig1\_20.jpg" is available in "jpg" format from:

<http://arxiv.org/ps/astro-ph/9903307v2>

This figure "fig1\_21.jpg" is available in "jpg" format from:

<http://arxiv.org/ps/astro-ph/9903307v2>

This figure "fig1\_22.jpg" is available in "jpg" format from:

<http://arxiv.org/ps/astro-ph/9903307v2>

This figure "fig1\_23.jpg" is available in "jpg" format from:

<http://arxiv.org/ps/astro-ph/9903307v2>

This figure "fig1\_24.jpg" is available in "jpg" format from:

<http://arxiv.org/ps/astro-ph/9903307v2>